On-board axial detection of wake vortices using a 2-µm LiDAR

Damien Douxchamps, *Member, IEEE,* Sébastien Lugan, *Member, IEEE,* Yannick Verschueren, Laurence Mutuel, Benoît Macq, *Senior Member, IEEE* and Kunihiro Chihara, *Senior Member, IEEE*

***Abstract*— This paper describes the first successful attempt to detect wake vortices axially using an on-board infrared pulsed Doppler LiDAR (Light Detection And Ranging). On-board axial detection is more complex than the classic ground-based tangential approach, because the axial air speed in vortices is low and the atmospheric particle density is reduced, yielding a poorer SNR. To provide meaningful results in such unfavorable conditions we have developed a new flexible signal processing method based on a two-primitive model fitting the spectrum of the Doppler return. This new spectral estimation successfully detects wake vortices with an admissible SNR that is lower than other on-board state-of-the-art approaches. It was validated through flight tests.**

***Index Terms*— Doppler LiDAR, wake vortex, spectral estimation.**

I. Introduction

WAKE vortices are rotating air masses generated by aircraft as a result of their bearing pressure. These air flows induce a rolling moment in a following aircraft entering them, creating a hazard particularly during take-off and landing phases. The rotating speed induced by a wake vortex in these phases is more important than in cruise phase and the aircraft may not have the resources to recover from such an encounter. Investigations on wake vortices started in the 1940s with the work of the Russian scientist Belotserkovsky [1], who later made it a personal challenge to better understand this phenomenon after the death of Yuri Gagarin, thought to have been caused by a wake vortex encounter in 1968. The dynamic behaviour of wakes is now well understood, and experiments have confirmed the theoretical advances. However, the practical impact of these advances is limited, and wake hazard together with weather conditions are still driving the separation distance of landings and the period between take-offs. These restrictions affect the throughput of today's close-to-saturation airports [2]. A system allowing a shorter period or a smaller separation distance, while maintaining the safety level, would therefore yield benefits for airports and reduce the need for unpopular new installations.

The periods or distances between aircraft movements are currently fixed by the International Civil Aviation Organisation (ICAO) regulations, and depend on the leading and following aircraft weights (implementation of these rules by the Federal Aviation Administration (FAA) can be found in [3] [4]). In practice, observations show that these rules are adapted by Air Traffic Control (ATC) personnel to reach optimum throughput. For example, a crosswind moving a vortex away from the trajectory of a following aircraft can lead to reduced separation distance between planes. This adaptation is made with the expert judgement of the air traffic controllers, but it is nonetheless "on a case-by-case basis" and is stressful for operators and pilots. A more systematic approach based on in situ measurements is therefore sought. In the recent years, ground Doppler Light Detection And Ranging (LiDAR) systems have been deployed in large airports to detect vortices near the runway threshold [5] [6] [7] [8]. These systems have a very good detection capability, since they scan in the transverse plane of the vortex where wind speeds are the highest. However, their measurement is local: it does not cover the entire approach corridor. This partly explains why on-board systems are being contemplated to directly warn pilots [9] and to be one of the components to airport-wide wake vortex management.

On-board integration of a LiDAR system was demonstrated in [10] and since then has been the subject of several studies, from atmospheric particle backscatter experiments [11] [12] to in situ measurements of wake encounters [13] [14]. The European Commission funded I-WAKE project, which will be described here, is however the first to test an operational on-board LiDAR-based axial detection of wakes.

This paper is organised around the data collected during two test campaigns. The first is a series of preliminary ground tests performed by the M-FLAME project in 2000 [15]. The primary goal of this campaign was to study the feasibility of axial vortex detection. This paper uses the M-FLAME data set for the purpose of testing our new signal processing algorithms for wake detection.

The second part of this paper uses the data collected in 2004 during the flight tests of the I-WAKE project. Two major differences exist between ground and on-board systems: (i) the aircraft is a moving platform and its position, speed and attitude must be compensated for; (ii) the return signal is noisier as measurements are taken at an altitude of 6000 feet where particle density is lower than at ground level. The present association of a new spectral model with the flight tests of the I-WAKE project provides the first proof of the feasibility of wake vortex on-board detection with an infrared LiDAR.

The authors are with the Université catholique de Louvain, Laboratoire de Télécommunications et Télédétection, Thales Avionics and the Nara Institute of Science and Technology, Image Processing Laboratory.

This work was supported by the European Commission as the I-WAKE project, contract number G4RD-CT-2002-00778, project number GRD1-2001-40176. The spectral analysis of the ground-based LiDAR signals uses data from the M-FLAME project, also funded by the European Commission under contract number BRPR96-182.

II. Wake vortex detection with a Doppler LiDAR

The underlying principle of operation of the vortex detector is the Doppler effect. A Doppler LiDAR will be able to distinguish a vortex from the rest of the atmosphere as the wind speeds inside a vortex are different from those in its more static surrounding environment. The Doppler effect itself describes the frequency shift Δs of a received signal due to the relative speed v of the transceiver and the local air mass:

$$\Delta s = \frac{-2v}{\lambda} \tag{1}$$

where λ is the wavelength of the emitted signal. This relation is only valid along the axis of propagation joining the receiver and emitter, and it is therefore only possible to measure the component of the air speed vector along the line of sight.

The wavelength of the laser is selected with respect to the particle size to be observed, the absorption spectrum of the atmosphere and the eye safety of the system. For the experiments described here, a 2.022µm diode-pumped Tm:LuAG pulsed laser was used as the light source of the heterodyning system. Pulsed operation is necessary to obtain volumetric information, and also to avoid blindness when receiving hard target returns from the ground or other highly reflective objects such as clouds. The pulse width of 400ns limits the depth resolution of the system to around 75m.

Contrary to tangential vortex detection, which only needs a one-dimensional angle scan, axial detection of wakes requires the laser to be swept across a volume. This is achieved by a two-dimensional scan, as depicted in Fig. 1, and a proper range gating of the return signal. The sinusoidal scanning pattern is achieved by one mirror for the horizontal deflection and by two counter-rotating prisms for the vertical deflection. The two deflections form one full sinusoidal scan of 37 periods every 5.5s. The horizontal and vertical openings are respectively 12° and 3°. The average horizontal scanning speed is $2.2^\circ/\mathrm{s}$ and the maximal vertical scanning speed is $47^\circ/\mathrm{s}$. The beam is collimated and has a diameter of approximatively 50mm. The angle of view of the scanner is pointed towards the 3° glideslope. The Gaussian laser beam is made of 2mJ pulses sent every 2ms so that each complete scan comprises around 2500 laser shots. As each pulse travels at the speed of light, the speed distribution of the atmosphere at a specific distance from the LiDAR is obtained by processing the associated delayed signal return. The return signal can therefore be time-gated to obtain an analysis volume between 800m and 2375m. It is then digitised at a sampling rate of 128MHz. Each resulting time series $S^L(k)$ of shot L is then split into gates of 64 samples, which is roughly equivalent to a spatial range of 75m. To obtain better frequency resolution and stability, the chunks of the previous and next gates are concatenated to the current gate data, which effectively yields 19 overlapping range gates of 225m (192 samples), each separated by a distance of 75m. The data available for each range gate g are thus defined as:

$$\begin{cases} S_g^L(k) = S^L\left(64(g-1)\dots 64(g+1)\right) \\ g = 1\dots 19, L = 1\dots 2500 \end{cases} \tag{2}$$

Of the numerous scans measured by the M-FLAME project, four will be presented here. These tests are the same as the ones used by Keane [15] and correspond to the landing of a large A340-600, a heavy A300-600 Super Transporter, a light Fokker 100 and a medium A320.

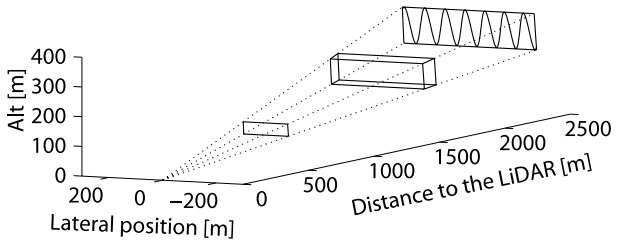

Fig. 1. The M-FLAME experiment configuration. The first gate is at a distance of 800m and the last at 2375m. The trace of the sinusoidal scanning is shown on the last gate. A typical volume of analysis for a range gate is presented at a distance of 1500m.

III. Building the spectra

As the aim is to estimate the Doppler shift of the return signal, our analysis is based on the signal power spectrum [16], which is obtained using a Fast Fourier Transform (FFT) on the signal $S_g^L(k)$:

$$P_g^L(k) = \left\| FFT\left(S_g^L(k)\right)\right\|^2 \tag{3}$$

Another less intuitive option is to analyse the signal correlation, which can be performed directly on the samples $S_g^L(k)$. Among the time-domain techniques available, the Auto-Regressive-Moving-Average (ARMA) has been tested on the M-FLAME data but did not provide satisfactory results because the shape of the spectral modes is not Gaussian [17].

Analysing the power spectrum $P_g^L(k)$, the mean returned frequency will reflect the Doppler shift and therefore can be used to provide the mean wind speed along the line of sight. As every wind speed will yield a different Doppler shift, the variance of the signal is an indication of the breadth of the speed distribution in a certain volume (for a more complete discussion of broadening effects see [18]). Since vortices are not laminar flows, we can expect to detect them by considering not only mean speed variations (Doppler shift) but also larger spectrum variances (wider peaks).

Formally, the signal spectrum mean f and variance σ correspond to the spectral moments of order one and two. The estimation of these moments is well described in the literature. The most complete description of spectral estimation applied to wind measurements is provided by Doviak and Zrnic [19]. Zrnic also proposes a study of range weighting [20] and a discussion of the particular case of pulse pairs [21], among others. Frehlich details a method for estimating the wind velocity statistics in a stationary atmosphere [22], which essentially uses the same spectral estimation techniques. Dias et al. also discuss improvements in spectral estimation of the moments for the case of a Gaussian signal in Gaussian noise [23] [24] [25]. The broad coverage of the subject allows us to concentrate here on the practical aspects of spectral estimation for vortex detection, taking the work of Keane [15] as a starting point.

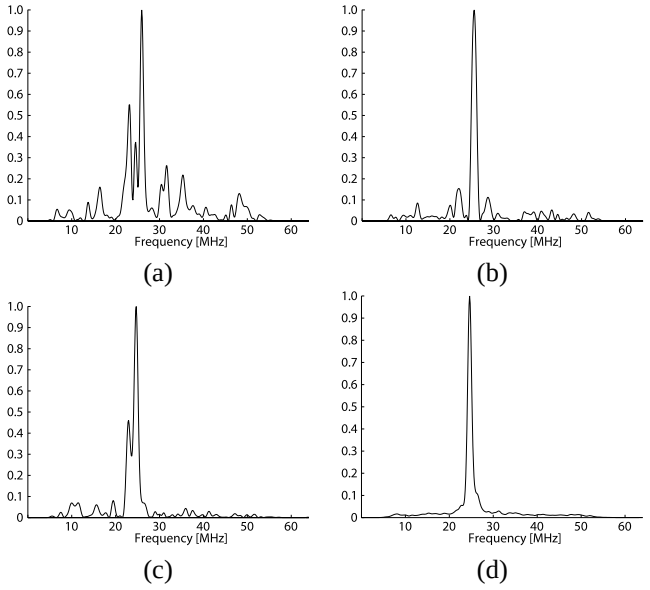

Fig. 2. Comparison of the spectra obtained with and without averaging. (a), (b), (c): individual spectra from a close range gate. (d): typical signal spectrum obtained with a weighted spectral averaging. The maxima of all spectra are normalised.

The spectra obtained from (3) are subject to local fading, are noisy and can depart significantly from a single Gaussian shape as can be seen in Figs. 2a-c. Attempts to estimate the spectral moments f_g^L and σ_g^L on these raw spectra $P_g^L(k)$ will therefore lead to spurious estimates [15]. Instead of first calculating the moments and then aggregating the results, we choose to apply these processing steps in reverse order (see for example [26]): we first average the spectra of several Lines of Sight (LOS) and then calculate the moments on this averaged spectrum. We also move the data to a regular grid by choosing resampling points located on a regular lattice of size 80×20 with horizontal and vertical coordinates i and j. However, one cannot simply average the spectra by summing them point to point, because each spectrum is Doppler-shifted by a different amount. Summation would then result in a broader peak than is actually observed. To avoid this, the spectra within the sampling radius r=0.3° are shifted to the median position $k_{g,med}(i,j)$ of their peak frequencies k_g^L before averaging them. The average is then weighted with an approximative estimation W_g^L of the signal quality to further improve the final spectrum:

$$W_g^L = \frac{P_{g,M}^L - P_{g,m}^L}{P_{g,M}^L} \tag{4}$$

where $P_{g,M}^L$ is the power spectrum peak value and $P_{g,m}^L$ is its average value. The resampled spectrum for image point (i,j) is thus expressed as:

$$P_g(i,j,k) = \frac{\sum\limits_{L\in r} W_g^L P_g^L \left(k - k_g^L + k_{g,med}\,(i,j)\right)}{\sum\limits_{L\in r} W_g^L} \tag{5}$$

A typical resulting spectrum is presented in Fig. 2d and shows that averaging the spectra provides a better basis for estimation of the spectral moments with fewer secondary peaks and a clear broadening of the main peak. This allows more accurate model matching, which in turn yields more information about the atmosphere.

Before addressing the estimation of the spectral moments, we note that it is possible to extract the noise component from the stable spectrum obtained from (5). It can be shown that the power of the reference signal at the detector can reach the point where most noise will come from the shot noise of the reference signal on the detector [27]. This noise therefore has a constant spectrum which can be estimated once by acquiring data with a direct laser feedback. The noise spectrum can then be removed from the observed spectrum to enhance extraction of the spectral parameters. The noise spectrum can also be part of the spectrum model, which is the approach presented below.

IV. Model-based spectral estimation

Direct estimation of spectral moments is widely covered in the literature. Estimation of the mean velocity is described in [28] [29] and [30], while Zrnic also discusses retrieval of the spectral width in [29] and [31]. Another approach to spectral estimation is to match a spectrum model to the received signal using non-linear fitting techniques [32]. Using this model-based technique, we first present the results of a single-primitive fit and then show that a new two-primitive model is more appropriate and has better discriminating capability for wake vortices.

A. Single signal primitive

A typical observed spectrum $P(f)$ such as the one shown in Fig. 2d has two identified components in the literature: the returned signal and the detector noise. The returned signal can be modeled as a Gaussian curve with a mean frequency f_1 and a variance σ_1 (see for example [32] [33] [34] and [35]). As far as detector noise is concerned, its spectrum $N(f)$ is known from specific measurements (see Section III above). However, an automatic gain control circuitry (AGC) was used before the signal digitization so that the amplitude n of the noise spectrum must still be determined. The simplest model for the signal spectrum is therefore

$$m_1(f) = me^{-\frac{(f_1-f)^2}{\sigma_1^2}} + nN\,(f) \tag{6}$$

where m is the amplitude of the signal peak. The spectrum is further normalised to reduce the degree of freedom of the model, leading to the following simplified expression:

$$M_1(f) = \frac{e^{-\frac{(f_1-f)^2}{\sigma_1^2}} + nN\,(f)}{1 + nN\,(f_1)} \tag{7}$$

where n is the relative noise level. Two resulting fits are presented in Fig. 3. The main peak of the spectrum is correctly modeled, but the fit is not accurate at its base: not only is the variance insufficient, but the spectrum also shows a clear asymmetry that cannot be accounted for with the current model.

The resulting spectral width σ_1 is presented in Fig. 4. The successive range gate images obtained are shown, starting from

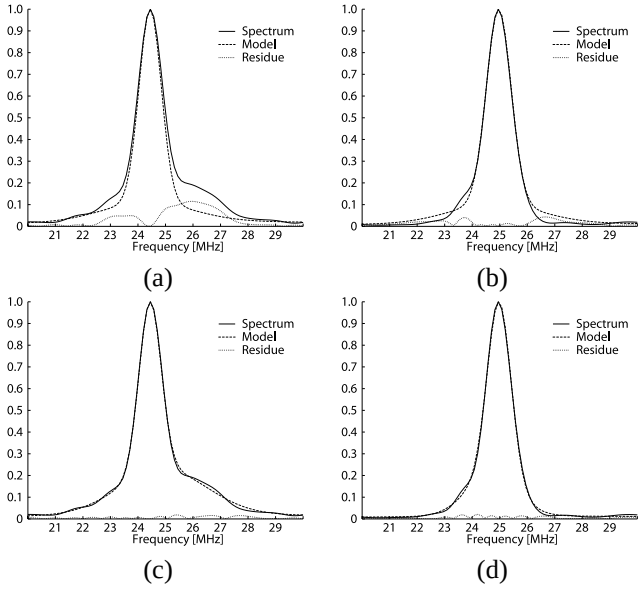

Fig. 3. Comparison of spectral fits obtained with a single signal primitive (a,b) and two signal primitives (c,d). The maxima of all spectra are normalised.

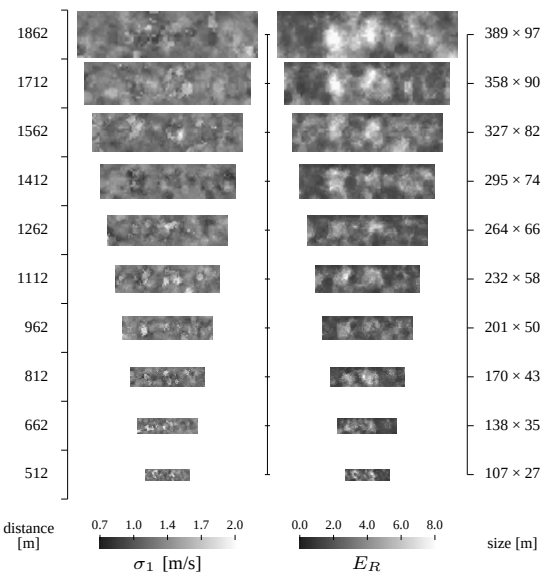

Fig. 4. Estimated parameters for the single-primitive model: spectral width σ_1 and residue energy E_R. The range gate distance refers to the range gate center. The fact that the vortices are visible on the residue energy confirms the inadequacy of the single-primitive model.

the farthest one (top) down to the nearest one (bottom). Each gate image can be seen as a vertical slice of the conic viewing volume, each point of the slice being located at a constant distance from the LiDAR. The use of an angular scan explains why the nearer gates have a higher spatial resolution (but are smaller) than the farther gates. The axial detection uses the turbidity of the vortex regions to detect them. Turbidity appears as a wider spectrum as it corresponds to a wider range of air speeds. Since we are scanning the vortices almost (but not perfectly) along their axis, residual projections of the tangential wind velocities in the vortex also contribute to the spread of the return spectrum. Two long parallel features should be visible on the spectral width results of Fig. 4, one for each vortex generated by the aircraft. However, the spectral width differs significantly from the estimations of Keane [15], with vortex signatures that can barely be seen. (An example of good signatures is presented later in Fig. 7.) This absence is explained by observing that all the broadening information is located at the base of the peak, where the quality of the fit of the Gaussian curve is poor (Fig. 3a). The second result provided in Fig. 4 is the residual energy E_R between the observed spectra $P(f)$ and its model $M_1(f)$:

$$E_R = \int \|M_1(f) - P(f)\| \, df \tag{8}$$

Since no metric was available for the energy of the observed spectrum due to the AGC, energy-related results will be presented without units throughout this paper. Observation of Fig. 4 reveals that the residue is the best way to detect the vortex activity, thereby clearly indicating that the single-primitive model is not complete. We therefore conclude that the single Gaussian model is not appropriate and that a second component must be used to take the broadening of the peak into account.

B. Two signal primitives

Given the insufficiency of the single-primitive approach, an additional Gaussian curve is added to model the base of the spectrum peak. This curve has a relative amplitude s_2, a variance σ_2 and a mean frequency f_2. We call this new component the secondary return and obtain a new normalised model:

$$M_2(f) = \frac{e^{-\frac{(f_1-f)^2}{\sigma_1^2}} + s_2 e^{-\frac{(f_2-f)^2}{\sigma_2^2}} + nN(f)}{1 + s_2 e^{-\frac{(f_2-f_1)^2}{\sigma_2^2}} + nN(f_1)} \tag{9}$$

Fig. 3c-d show the results of this two-primitive fit on the same spectra of Fig. 3a-b. The base of the main peak and the main peak itself are now much better modeled. The residue is very small compared to the original single-primitive approach and consists almost entirely of small noise variations. This indicates the new model is meaningful and that the spectrum should indeed be modeled by two Gaussian curves of different mean, level and variance.

A full description of the parameter variation is provided in Figs. 5 and 6. Let us comment on each parameter one by one:

- **Mean velocity, main primitive $\mathbf{v}_1$ or $\mathbf{f}_1$**: the mean frequency f_1 is here represented by the associated wind velocity v_1 obtained with (1):

$$v_1 = \lambda \frac{f_1 - f_l}{2} \tag{10}$$

  where $f_l(i,j)$ is the laser frequency, estimated by direct sampling of the emitted pulse. This result is almost identical to the single-primitive model, which is not surprising since the latter was already able to fit the main peak correctly.
- **Spectral width, main primitive σ_1**: the spectral width of the main peak, also converted to velocity measures, is

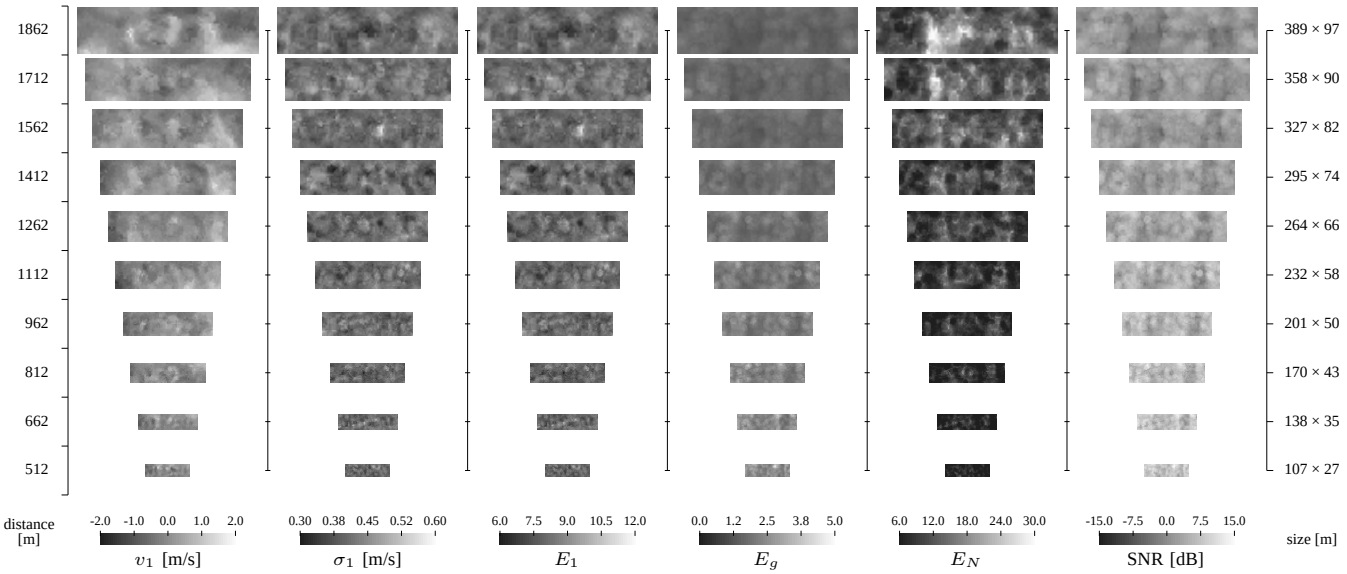

Fig. 5. Estimated parameters for the two-primitive model. The first four columns describe the main primitive: its mean velocity f_1, spectral width σ_1, energy E_1 and global return signal energy E_g. The noise component is described only by its relative energy E_N. The last column shows the SNR defined in (12).

completely decorrelated from the vortex signature. This shows that the main Gaussian component is not suitable for vortex detection with spectral width measurements.

- **Relative energy, main primitive $\mathbf{E}_1$**: since we are working with a normalised spectrum, the energy is directly proportional to the peak variance, leading to similar results for E_1 and σ_1.
- **Relative amplitude, secondary peak $\mathbf{s}_2$**: the relative amplitude of the secondary return bears only a small correlation with the vortex location. It will be used below in the form of the secondary return energy.
- **Mean velocity, secondary primitive $\mathbf{v}_2$ or $\mathbf{f}_2$**: the mean frequency (or wind velocity) of the secondary signal is similar to that of the main signal. This velocity is more corrupted by noise in the far field because the relative amplitude of the secondary component is close to the amplitude of the noise spectrum variations in this region.
- **Spectral width, secondary primitive σ_2**: the vortex signatures are clearly visible, showing again that only the secondary return signal contains valid information about their higher turbidity.
- **Relative energy, secondary primitive $\mathbf{E}_2$**: the vortex signatures are also clearly detected. The response of this parameter is more polarised (high or low values, with few intermediate ones), but has fewer parasitic detections than σ_2 in the far field. This energy coincides with the vortex location and the secondary peak is only present where a vortex is located. It can be thus considered as the signature of a vortex. Note that we are able to capture larger spectral variances than [15], and the range maximum has consequently been extended to 3m/s.
- **Relative noise energy $\mathbf{E}_N$**: defined as

$$E_N = n \int N(f) df \tag{11}$$

Although the *absolute* noise energy is not dependent on the distance to the laser source, E_N represents the noise energy *relative* to the signal peak, as described by (9). As such, E_N is expected to increase when the signal peak decreases with the distance to the LiDAR, which is observed in Fig. 6. Radially-aligned features appear on this set of gates as well as for other model parameters. These features are not vortices, which have a parallel alignement, but are due to fluctuations in the energy of the emitted pulse.

- **Relative signal energy $\mathbf{E}_g$**: the received power is not homogeneous, as stated above, and also decreases with distance from the laser. Zones where it is higher correspond to a lower relative noise energy.
- **SNR**: the signal-to-noise ratio is defined in dB as

$$SNR = 10log\frac{E_1 + E_2}{E_N} \tag{12}$$

- **Relative residue energy $\mathbf{E}_R$**: as expected, the residue is much lower than in Fig. 4, confirming that the two-primitive approach is better than the single-primitive one.

The estimated values of these parameters are obtained by fitting the spectrum model to the observed data using a non-linear iterative process, in our case a Gauss-Newton method with a Levenberg-Marquart-type adjustment. *A priori* knowledge of the vortex parameters has been integrated in the form of limited variation domains for each parameter. This limitation is particularly important for the variances of the Gaussian primitives, which must have mutually exclusive variation domains for the algorithm to converge properly. The values used empirically are $\sigma_1 \in [0.25, 1.25]$MHz and $\sigma_2 \in [1.5, 7.5]$MHz. The result is a convergence that is relatively fast, requiring less than 30 iterations. In a few cases the convergence is not achieved, especially in the far field, which has more variability due to a higher noise level. However, this is limited to about 0.5% of the worst-case farthest gate and is not visible in the final results.

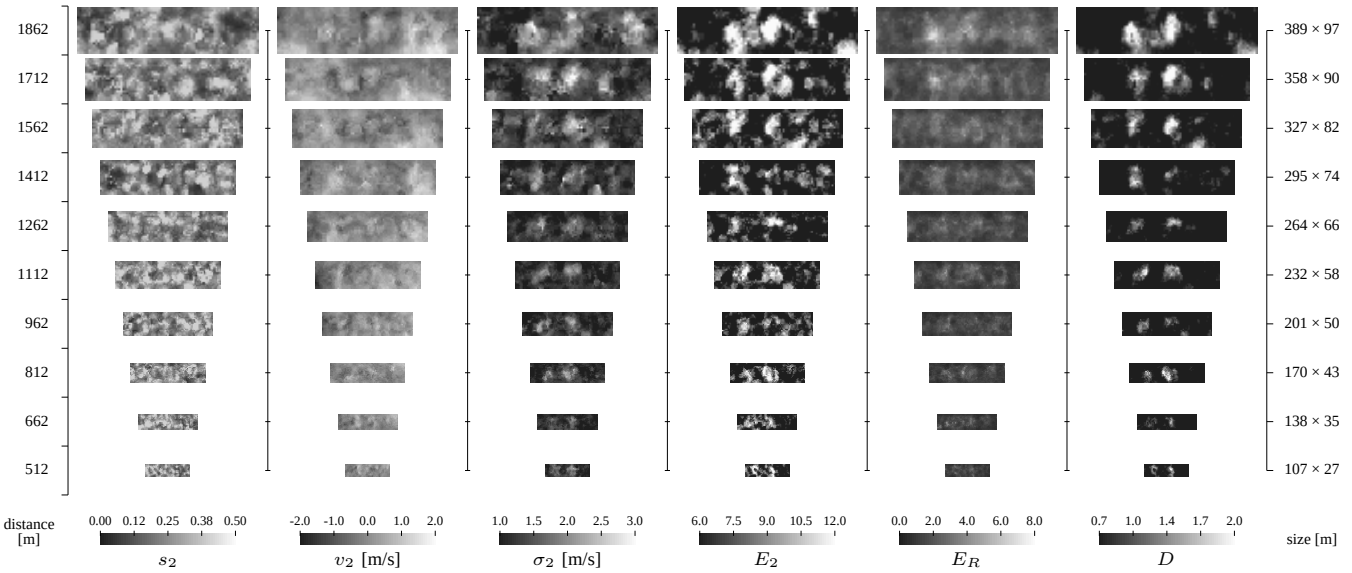

Fig. 6. The model parameters of the secondary primitive: its relative amplitude s_2, mean velocity f_2, spectral width σ_2 and energy E_2. The last two columns show the residual energy E_R and the detection field D.

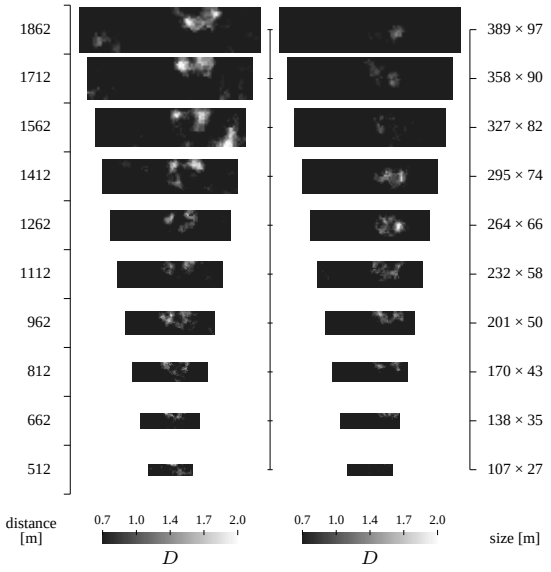

Fig. 7. The final detection field D of the two-primitive model-based vortex detection for two other reference flybys: the A300-600 Super Transporter (left) and Fokker 100 (right) M-FLAME tests.

From this discussion of the variation of the model parameters, we conclude that a good candidate for the detection of wake vortices would be to combine the secondary peak energy and variance into a single detection field $D(i,j)$:

$$D(i,j) = \sigma_2(i,j)E_2(i,j) \tag{13}$$

The resulting detection field is shown in Fig. 6 and in Fig. 7 for two other flybys. The overall performance of the new detector is better from several aspects. First we note the higher contrast between vortex and atmosphere zones, which, together with the lower noise, results in a greater usable range for the LiDAR than was presented in [15]. The results for the landing of the Fokker 100 (Fig. 7, right) also show that we are able to detect weaker wakes, even in the far field and without any parameter tuning, thanks to the superior discriminating power of the two-primitive model. Inspection of the SNR and D fields reveals that the minimum SNR for a good detection lies between -5dB and -10dB, while the threshold found by Keane in [15] was 0dB. Another advantage of our approach is that this SNR is available for each estimation of the detection field. It can be used as a weight in (13) to automatically adapt the detection to lower SNR situations that might otherwise trigger unwanted alarms in the cockpit. The residue energy can also be used for the same purpose. On a broader scope, the two primitive model provides more information about the atmosphere and may be used to detect other atmospheric hazards which would have a different signature on the several parameter fields.

C. Physical interpretation

We have observed that in the ground data set of the M-FLAME project noisier spectra were found not only in the case of local fading but also when the LOS was intersecting the vortex. The spectra show a similar multiple-peak pattern in both cases (Fig. 2). However, the strength of the return signal is likely to be higher in the case of an intersection with a vortex, so that spectra affected by local fading will not have a significant negative impact on the averaged spectrum. In this context, the combination of neighbouring LOSs will create a secondary Gaussian component when multiple small peaks are averaged to form a wider spectral base for the primary return. This does not by itself justify the shape that we have chosen for the secondary return. However, given the poor SNR with which we are working, a simple model is necessary, and the Gaussian curve provides satisfactory results.

Altough this vortex detection technique is based mainly on axial wind speeds within the vortex, the tangential component still affects ground and airborne detection favourably for two reasons. First, we cannot guarantee a perfectly axial view of

the vortex. This is a minor problem for the ground tests, which in fact are very well aligned. For airborne flight tests, however, obtaining a good alignment would require the measuring aircraft to fly below the vortex pair, a significant safety issue (see Section VI). Second, the use of an angular scan on two parallel features like wake vortices means that it is impossible to align all LOSs with the vortex axis. For instance, if the vortex is aligned with a LOS on the left of the scanning volume, then a LOS on the right will be several degrees off the vortex axis (12° in the case of our tests). Overall, since alignment is not perfect, the large tangential component of the wind speed can and will be used for vortex detection in addition to the axial component.

Finally, our own simulations of LiDAR and vortex interactions have confirmed the presence of a secondary Gaussian component in the return signal in the case where the spectra of several neighbouring LOSs are averaged [36]. Those results also show that the secondary component is present only in the vortex region and thus allows the detection of wake vortices.

V. Spectral estimation of on-board signals

After development of the signal processing algorithms and their testing on ground-based LiDAR data, the next step was to perform flight tests with an airborne LiDAR. We will first describe this installation. The flight tests are then depicted, followed by a discussion on the necessary signal processing adaptation compared to the ground system used in the previous section.

A. Aircraft installation and flight tests

Installation of the LiDAR in the aircraft is performed under several constraints. First, for safety reasons, the equipped aircraft must not encounter the vortex generated by the airplane in front of it. As wakes move downwards with time, the altitude of the following aircraft must be equal to or higher than that of the generating aircraft. During flight tests, the measuring aircraft also follows the generating aircraft so that the vortices can be detected axially, in a configuration as close as possible to a real approach. This forces the forward-looking LiDAR to aim downwards, in the direction of the flight path. The second limitation comes from the aircraft itself which has no opening on its underside to allow the laser beam to aim straight forward along the fuselage axis. As an additional hole cannot be made in the fuselage, we have modified one of the lateral windows and designed a protruding fiberglass fairing to protect the scanner optics. For aerodynamic reasons the fairing could not extend far outside the airplane; as a result, the LiDAR did not aim straight ahead but with a small angle offset from the longitudinal axis. These vertical and horizontal angles α and β are represented in Fig. 8 and both have a value of 9°.

The flight tests were conducted in the vicinity of Toulouse-Blagnac airport at the end of June 2004, with an A340-600 as generating aircraft. The flight plan included a zig-zag route to be followed by the measuring aircraft behind the straight flight path of the A340-600. This approach almost guaranteed that the vortex would intersect the analysis volume, although it also meant that the vortex would be visible only for a few scans at each pass.

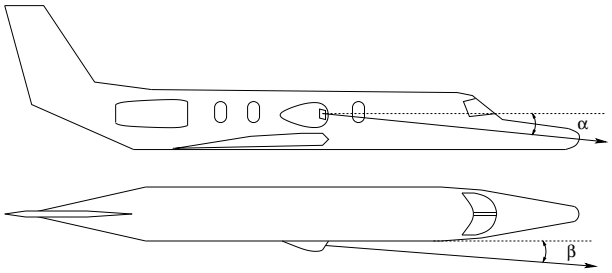

Fig. 8. Installation of the LiDAR on board the NLR Citation II aircraft. Angles α and β are the mean gazing angles of the LiDAR relative to the fuselage axis.

B. Signal processing adaptation

From a signal processing point of view, the adaptations necessary for an on-board system are limited to the speed, attitude and position of the plane, which must be integrated into our algorithms. However, the operational conditions also require an adaptation of the model-based approach for the lower SNR that is experienced at a higher altitude.

1) Position and attitude: The movement of the laser source means that every shot is issued from a different point in space. Due to the relatively high speed of the aircraft (80m/s), the difference in position between the first and last shot of a scan is 80m/s$\times$5s=400m, which is a significant displacement compared to the LiDAR range of 2360m. To compensate for this motion and for the aircraft's attitude, all the LOSs of one scan are placed in a single reference system (in this case the reference frame of the aircraft when the last LiDAR return was acquired). The bundle of LOSs is then truncated by near and far boundaries of 800m and 2360m, respectively. This truncation reduces the volume of analysis but guarantees geometrically coherent results.

2) Speed: In a Doppler system, the relative speed of the source and the target creates the frequency shift. The speed of the aircraft therefore has a major impact on the results and must be integrated into the signal processing. This is especially true because both speeds have the same weight in (1), so that a variation of 1% in the aircraft speed (0.8m/s) corresponds to nearly 25% of the airspeed variations due to a vortex (which are roughly within $\pm$3m/s). The direction of each LOS must also be taken into account for this compensation since the LiDAR measures air speed vectors along the LOS only.

3) Adaptation to the lower SNR: The aerosol concentration at the altitude of the flight tests is much lower than on the ground, leading to a lower reflected and received power than observed during the M-FLAME tests. As the noise level at the detector is constant, the global SNR of the sampled signal will decrease. Given the low SNR of -25dB to 0dB observed in the flight, test data one must carefully integrate the noise component into the spectrum model. For the gate closest to the observing aircraft (980m), the noise spectrum can be considered flat with respect to the amplitude of the main return peak (Fig. 9a). These spectra are similar to those of the

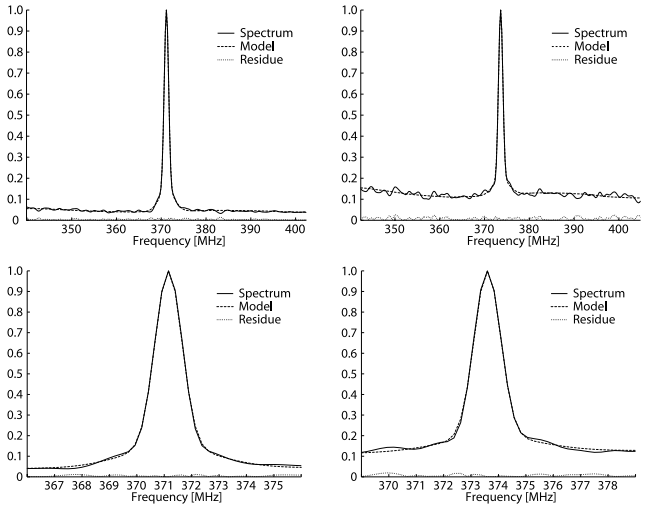

Fig. 9. Spectral fits of on-board signals with a two-primitive model for range gates 1 (a, 980m) and 7 (b, 1700m). The maxima of all spectra are normalised. Lower graphs show a zoom on a limited frequency range around the central peak of the upper graphs. The first spectrum (a) has a noise floor that is significantly higher than what was observed for the ground tests in Fig. 2d, even though (a) is from a close range gate.

ground tests. However, as the analysed gate is located further away from the aircraft, the SNR decreases rapidly and the larger noise component amplitude can no longer be considered constant across the spectrum. A typical spectrum at a distance of 1640m is presented in Fig. 9b. Its higher noise level prevents the detection of the secondary signal component and also leads to noise in the estimated spectral width of the main peak.

As explained in Section III, the shape of the noise spectrum is constant over the scans, so that only the amplitude factor varies. It is thus logical to estimate this spectrum and use it in the same way as in the ground tests. However, no specific noise-spectrum shots were taken during the I-WAKE flight tests because the laser was started after take-off and no such tests could be performed in flight. Furthermore, tests done before take-off would not accurately describe the noise spectrum, as the laser changes its characteristics depending on factors such as aircraft altitude and vibration levels. For these reasons, the noise spectrum is estimated from the last samples of the LOS. These samples correspond to a distance of a little more than 5km from the aircraft, which is outside the useful range of the LiDAR. The corresponding data should therefore only contain noise whose spectrum is estimated for every LOS and then averaged over the whole scan to obtain stable data. This approach is more time-consuming than the off-line estimation made in the ground-based tests, but has the advantage of automatically adapting every 6s to changes in the detector noise spectrum that might occur during the flight.

Finally, the lower SNR requires that we adapt two parameters specified for the ground tests: the gate length is now set to 120m to ensure a better basis for the FFT, and the resampling radius r is set to 0.7° to include more shots in the spectrum aggregation. As this radius is significantly higher than for the ground tests, the resolution of the range gate images is halved to 40×10 points.

C. Geometric estimation of the vortex positions

We performed a geometric estimation of the vortex positions in the scanned volume to provide more confidence in our results. These estimations use the all geometric measurements available, including the position and attitude of both the generating and following aircrafts, their speed, and the angles of regard of the LiDAR scanner. An estimate of the wind speed vector (23kt, 291°) was also used to obtain the correct lateral displacement of the vortices. However, the wind has little influence on our measurements because it was almost aligned with the track of the generating aircraft. For the vortex descent rate, we used the following expression that yields a result close to the commonly applied value of 1m/s:

$$w_{sink} = \frac{\Gamma}{2\pi b_0} \approx 0.96 \tag{14}$$

where the circulation Γ was set to 300m^2/s, b_0=πb/4 and b=63.45m is the aircraft wingspan. The results of this geometric estimation are presented in the final results as circles (Figs. 10 to 12). The diameter of each circle does not reflect the true zone of influence of the vortex; it has been selected based on visualization criteria only. Estimations for the vortex age and for the laser-vortex misalignement (6° vertically and horizontally) were also obtained using the geometric estimation of the vortex positions.

VI. Airborne results and discussion

The results of each model parameter are presented for the scan 07-23 (2GB-block number 7, scan 23) in Figs. 10 and 11. A time evolution of the vortex is shown in Fig. 12 for scans 09-09 to 09-14. Like the ground results, the nearest gate is shown at the bottom. The distance to the airplane increases by steps of 120m moving from the bottom to the top of the figure. The center of the nearest gate is located at 980m, and that the farthest is at 2060m.

Two vortices should be visible in the detection field of Fig. 11, because the gate size is much larger than the vortex separation distance. We observe this for gates 4 to 6, although the strength of the two vortices is dissimilar. On those three gates the vortices are roughly parallel, as expected, and fit their geometrically-predicted positions.

Compared to the ground tests (Figs. 5 and 6) we note that the parameters are noisier; this is expected given the lower SNR, which is now at best 0dB. As noted in Section IV-B the detection capability quickly degrades when the SNR is below -10dB, which here corresponds to a distance of 1580m or gate 6. The detection field of Fig. 11 confirms this -10dB threshold, as the first six gates are well rendered but from the seventh gate onward the results are significantly noisier. Due to the zigzag trajectory of the following aircraft, the vortices appear only in the range from 1300m to 2000m and within this range only three gates (4 to 6) have an acceptable quality. The necessity of good noise estimation is also more important than for the ground tests as the noise (and its power variations along the spectrum) is relatively more important and quickly

masks the useful signal if not modelled properly. Tests have shown that, using a simpler flat noise spectrum, the quality of the results degrade much faster and no detection can be made at all.

The observed mean speed deficit is more intense than for the ground tests. This is due to the larger misalignment between the vortex and the scanning axis, which leads to the tangential component being taken into account in the measurements (see Section IV-C). Indeed, the space between the two vortices contains air moving downwards; this air mass will appear as moving away from the aircraft, when seen from above from the following plane. The mean speed deficit also occurs over a wide range, which shows that we are looking at a well-formed vortex section, before its turbulent breakdown. The age of the vortex was estimated using geometric simulations, and ranges from 36s to 42s depending on the scan and gate. This age correlates with the simulations of Darracq, who observed that a vortex is axially detectable between 18s and 48s of age [37]. The present technique can thus work not only with almost pure axial data (as shown by the ground tests) but also if the following aircraft is not perfectly aligned with the vortex. However, our approach may not work in a purely axial configuration and when the observed vortex is very young [37]. Old vortices after turbulent breakdown will also be more difficult to detect, but they present a limited threat to the following aircraft.

Finally, Fig. 12 shows six successive scans across the vortex. Their apparent displacement to the left actually corresponds to the zig-zag pattern of the measuring aircraft, which was moving to the right at the time. The coherence of vortex detection is visible in both time and space. The limitation of the range of detection is also visible, as no vortex is detected beyond 1820m.

VII. Conclusions

In this paper we have presented a spectral estimation of on-board LiDAR signals, with the goal of detecting wake vortices in an axial fashion. Several methods and variations have been tested, using data collected during both ground and on-board test campaigns. Existing techniques in the literature fail to detect vortices reliably while the detector is airborne, but our new approach of two-primitive spectral modeling succeeds in this task. Our results also match the geometric estimation of vortex positions. The proposed spectral estimation has two major advantages over previous approaches. First, it allows correct detection at lower SNR, which proved to be essential for the analysis of on-board signals. Second, since the technique provides more information about the atmosphere, it could be used to detect other events like wind shear or clouds, although confirmation of this will require a more in-depth analysis. Further research is currently underway to address the implementation of our proposed technique in on-board computer platforms.

Acknowledgments

The I-WAKE consortium was composed of Thales Avionics (France), Airbus (Germany), the DLR (Germany), LISA Laser (Germany), the University of Hamburg (Germany), the NLR (Netherlands), Faunhofer IOF Jena (Germany) and UCL TERM (Belgium), all of which should be thanked for their indispensable participation in the project.

The authors are also grateful to Michael Keane for his help with the M-FLAME data and signal processing.

References

[1] W. Jackson, “Wake vortex prediction: An overview,” Transportation Development Center, Transport Canada, Tech. Rep. TP13629E, Mar. 2001.

[2] J. N. Hallock, C. Tung, and S. Sampath, “Capacity and wake vortices,” in *Proc. Intl. Congress of Aerospace Sciences (ICAS’02)*, Toronto, Canada, Sept. 2002, paper 7.9.1.

[3] *Air Traffic Control*. Federal Aviation Administration (FAA), 2004, no. 7110-65P, ch. 3-9-7.

[4] *Aeronautical Information Manual*. Federal Aviation Administration (FAA), 2004, ch. 7-3.

[5] J. M. Vaughan, K. O. Steinvall, C. Werner, and P.-H. Flamant, “Coherent laser radar in Europe,” *Proc. IEEE*, vol. 84, no. 2, pp. 205–226, Feb. 1996.

[6] D. A. Hinton, “An aircraft vortex spacing system (AVOSS) for dynamical wake vortex spacing criteria,” in *Proc. 78th Fluid Dynamics Panel Symposium*, Trondheim, Norway, May 1996.

[7] C.R.Tatnall, “An investigation of candidate sensor-observable wake vortex strength parameters for the NASA Aircraft Vortex Spacing System (AVOSS),” NASA, Hampton, VA, Tech. Rep. 206933, Mar. 1998.

[8] B. Lamiscarre, B. Christophe, C. Fournet, J. Lemorton, L. Poutier, and A. Oyzel, “Nouveaux capteurs pour l’amélioration de la sécurité et de l’efficacité des mouvements en zone aéroportuaire,” in *Proc. 5ème Journée AAAF*, Toulouse, France, Jan. 1999.

[9] W. L. Holforty and J. D. Powell, “Flight deck display of airborne traffic wake vortices,” in *Proc. Digital Avionics Systems Conf. (DASC’01)*, Daytona Beach, FL, Oct. 2001.

[10] T. J. Wagener, N. Demma, J. D. Kmetec, and T. S. Kubo, “2µm LIDAR for laser-based remote sensing: Flight demonstration and application survey,” *IEEE Aerosp. Electron. Syst. Mag*, pp. 23–28, Feb. 1995.

[11] D. Soreide, “Airborne coherent LIDAR for advanced in-flight measurements,” in *Proc. Conf. on Aviation, Range, and Aerospace Meteorology*, Orlando, FL, Sept. 2000, paper 8-18.

[12] R. Bogue, R. McGann, *et al.*, “Comparative optical measurements of airspeed and aerosols on a DC8 aircraft,” NASA, Edwards, CA, Tech. Rep. 113083, July 1997.

[13] D. Vicroy, J. Brandon, G. Greene, R. Rivers, G. Shah, E. Stewart, and R. Stuever, “Characterizing the hazard of a wake vortex encounter,” in *Proc. Aerospace Sciences Meeting and Exhibit (AIAA’97)*, Reno, NV, Jan. 1997.

[14] D. Vicroy, P. Vijgen, H.M.Reimer, J. L. Gallegos, and P. R. Spalart, “Recent NASA wake-vortex flight tests, flow-physics database and wake-development analysis,” in *Proc. World Aviation Congress and Exposition*, Anaheim, CA, Sept. 1998, paper 985592.

[15] M. Keane, D. Buckton, M. Redfern, C. Bollig, C. Wedekind, and F. Kopp, “Axial detection of aircraft wake vortices using doppler lidar,” *Journal of Aircraft*, vol. 39, no. 5, pp. 850–861, Sept. 2002.

[16] M. J. Levine, “Power spectrum parameter estimation,” *IEEE Trans. Inform. Theory*, vol. 11, pp. 100–107, 1965.

[17] D. Douxchamps, “Multidimensional photogrammetry of short-lived events,” Thèse de Doctorat, Université catholique de Louvain, Louvain-la-Neuve, Belgium, Oct. 2004.

[18] G. D. Nastrom, “Doppler radar spectral width broadening due to beamwidth and wind shear,” *Annales Geophysicae*, vol. 15, pp. 786–796, 1997.

[19] R. J. Doviak, D. S. Zrnic, and D. S. Sirmans, “Doppler weather radar,” *Proc. IEEE*, vol. 67, no. 11, pp. 1522–1553, Nov. 1979.

[20] D. S. Zrnic and R. J. Doviak, “Matched filter criteria and range weighting for weather radar,” *IEEE Trans. Aerosp. Electron. Syst.*, vol. 14, pp. 925–930, Nov. 1978.

[21] D. S. Zrnic, “Spectral moments estimates from correlated pulse pairs,” *IEEE Trans. Aerosp. Electron. Syst.*, vol. 13, pp. 344–354, 1977.

[22] R. Frehlich and L. Cornman, “Estimating spatial velocity statistics with coherent doppler lidar,” *Journal of Atmospheric and Oceanic Technology*, vol. 19, no. 3, pp. 355–366, Mar. 2002.

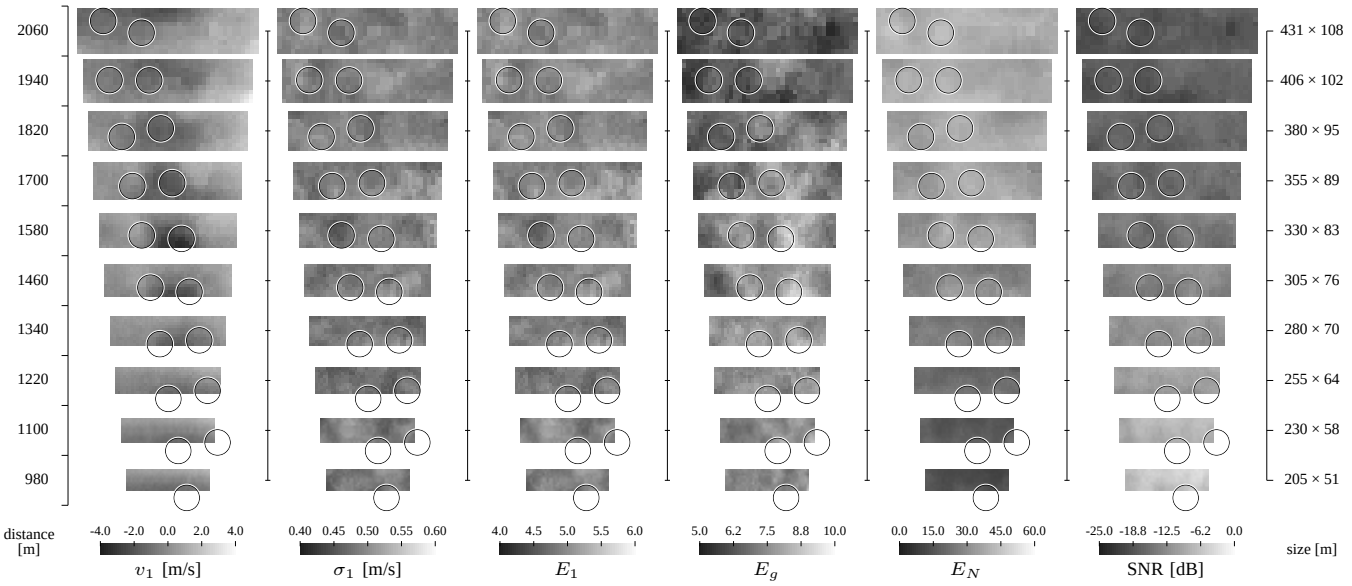

Fig. 10. I-WAKE flight test: scan 07-23. Parameters shown are the main primitive's mean velocity v_1, spectral width σ_1 and energy E_1, the global signal energy E_g, the noise energy E_N and the SNR. Note that the average SNR is 10dB below the one observed in the M-FLAME ground tests (Fig. 6).

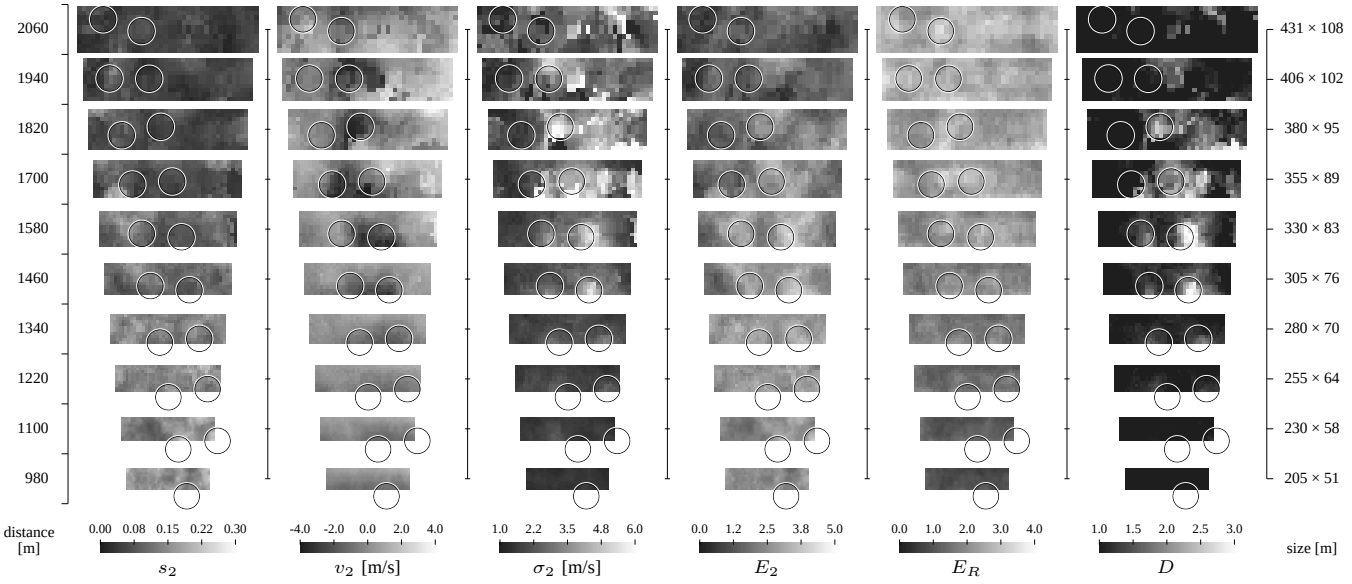

Fig. 11. I-WAKE flight test: scan 07-23. Parameters shown are the secondary primitive's level s, mean velocity v_2, spectral width σ_2 and energy E_2, the residual energy E_R and the detection field D.

[23] J. Dias and J. Leitão, "Asymptotically efficient estimation of spectral moments," *IEEE Trans. Acoust., Speech, Signal Processing*, vol. 43, no. 9, pp. 2222–2225, Sept. 1995.

[24] J. Dias and J. Leitão, "Nonparametric estimation of mean doppler and spectral width," *IEEE Trans. Geosci. Remote Sensing*, vol. 38, no. 1, pp. 271–282, Jan. 2000.

[25] J. Dias and J. Leitão, "Nonparametric estimation of mean velocity and spectral width in weather radar," in *Proc. Intl. Geoscience and Remote Sensing Symposium (IGARSS'95)*, vol. 2, Florence, Italy, Jan. 1995, pp. 2121–2125.

[26] H. Linné, "Heterodyne DIAL at high repetition rate," in *Proc. Intl. Laser Radar Conf. (ILRC'98)*, Annapolis, MD, July 1998.

[27] R. M. Huffaker and R. M. Hardesty, "Remote sensing of atmospheric wind velocities using solid-state and CO2 coherent laser systems," *Proc. IEEE*, vol. 84, no. 2, pp. 181–204, Feb. 1996.

[28] P. R. Mahapatra and D. S. Zrnic, "Practical algorithms for mean velocity estimation in pulse Doppler weather radars using a small number of samples," *IEEE Trans. Geosci. Remote Sensing*, vol. 21, no. 4, pp. 491–501, Oct. 1983.

[29] D. S. Zrnic, "Estimation of spectral moments for weather echoes," *IEEE Trans. Geosci. Electron.*, vol. 17, no. 4, pp. 113–128, Oct. 1979.

[30] E. S. Chornoboy, "Optimal mean velocity estimation for Doppler weather radars," *IEEE Trans. Geosci. Remote Sensing*, vol. 31, no. 3, pp. 575–586, May 1993.

[31] D. S. Zrnic, "Spectrum width estimates for weather echoes," *IEEE Trans. Aerosp. Electron. Syst.*, vol. 15, no. 5, pp. 613–619, Sept. 1979.

[32] S. Takeda, T. Nakamura, and T. Tsuda, "An improvement of wind velocity estimation from radar Doppler spectra in the upper mesosphere," *Annales Geophysicae*, vol. 19, pp. 837–843, 2001.

[33] R. D. Palmer, J. R. Cruz, and D. Zrnic, "Enhanced autoregressive moving average spectral estimation applied to the measurement of Doppler spectral width," *IEEE Trans. Geosci. Remote Sensing*, vol. 29, no. 3, pp. 358–367, May 1991.

[34] L. H. Jansen and G. V. der Spek, "The shape of Doppler spectra from precipitation," *IEEE Trans. Aerosp. Electron. Syst.*, vol. 21, no. 2, pp. 208–219, Mar. 1985.

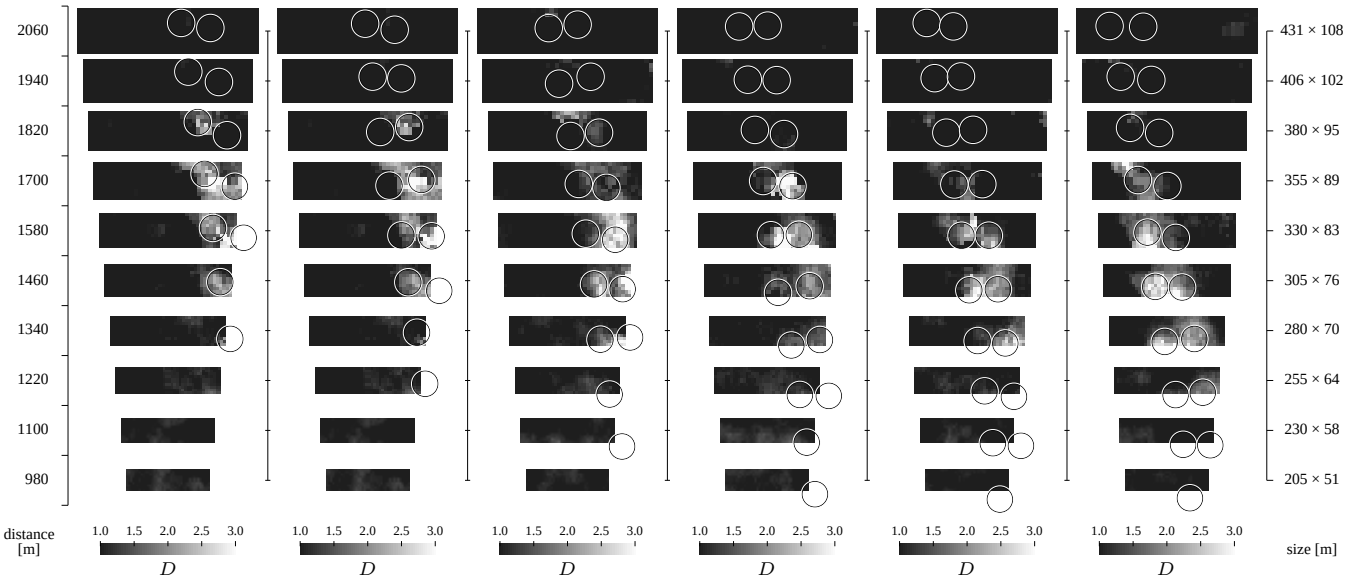

Fig. 12. I-WAKE flight test: time-evolution of the wake vortex detection for scans 09-09 to 09-14.

[35] R. Frehlich, "Effects of wind turbulance on coherent Doppler lidar performance," *J. of Atmospheric Science and Oceanic Technology*, vol. 14, no. 1, pp. 54–75, Jan. 1997.

[36] S. Lugan, L. Bricteux, B. Macq, G. Winckelmans, and D. Douxchamps, "Simulation of LiDAR-based aircraft wake vortex detection using a bi-Gaussian spectral model," in *Proc. Intl. Geoscience and Remote Sensing Symposium (IGARSS'07)*, Barcelona, Spain, July 2007.

[37] D. Darracq, A. Corjon, F. Ducros, M. Keane, D. Buckton, and M. Redfern, "Simulation of wake vortex detection with airborne Doppler lidar," *J. of Aircraft*, vol. 37, no. 6, pp. 984–993, Nov. 2000.

Damien Douxchamps received his PhD in Electrical Engineering from the Université catholique de Louvain in 2004. He was invited scientist at the National Taiwan University (NTU), Taiwan, and the Advanced Telecommunications Research Institute (ATR), Japan. He is currently assistant professor at the Nara Institute of Science and Technology (NAIST), Japan. His research interests include ocean engineering, robotics and 3D computer vision. He is a member of the IEEE and the Oceanic Engineering Society.

Sébastien Lugan received his master's degree and DEA in 2003 at the Ecole Supérieure d'Ingénieurs en Electronique et Electrotechnique, and the Gaspard-Monge Institute of Electronics and Computer Science, respectively. Since then, he joined the Communications and Remote Sensing Laboratory of the Université catholique de Louvain, where he is preparing a PhD thesis. His research interests include medical imaging, mega-image navigation and LiDAR detection of wake vortices.

Yannick Verschueren received his BEng Degree in Electro-Mechanical Engineering form the Université catholique de Louvain, Belgium in 2002. His is currently working in the design, test and certification of critical embedded software for the aeronautic industry.

Laurence Mutuel received in 1996 both her Master of Science from the University of California at Los Angeles and her Diplôme Ingénieur Grandes Ecoles from EPF in France. She continued at UCLA with a PhD in 2000 in Aerospace Engineering. She worked on guidance, navigation, fault-tolerant estimation and control for UAVs as part of the autonomous formation flight project. In 2002, she joined THALES Aerospace in France to coordinate atmospheric surveillance for turbulence detection systems and, in particular the I-WAKE project. She is now coordinating the R&D for airborne surveillance systems, including terrain, traffic and weather surveillance.

Benoît Macq is full Professor at the Université catholique de Louvain (UCL) leading a team of 40 researchers and engineers involved in image processing, communications and multimodal interactions. He is founder of 7 spin-offs companies. He has been Associate Editor of IEEE Trans on Image Processing and IEEE Trans on Multimedia, Guest Editor of "Signal Processing: Image Communication", Guest Editor of the Proceedings of the IEEE, Guest Editor of the IEEE Trans on Circuits and Systems for Video Technology. He is a member of the Image and Multidimensional Digital Signal Processing Technical Committee (IMDSP-TC) of the IEEE. Benoît Macq is appointed as the general chairman of ICIP 2011 and is Senior Member of the IEEE.

Kunihiro Chihara received the BS degree from Osaka University, Japan, in 1968 and the MS and PhD degrees in engineering science from Osaka University, Japan, in 1970 and 1973, respectively. He is currently a dean professor at the Graduate School of Information Science, Nara Institute of Science and Technology (NAIST), Japan. His research interests include medical ultrasonic imaging, signal processing, ubiquitous computing, and the application of multimedia. He is a member of ISCIE, JSMBE, JSUM and the IEEE.